Article

Double-Chamber Underwater Thruster Diaphragm with Flexible Displacement Detection Function

Chong Cao, Chengchun Zhang,* Chun Shen, Yasong Zhang, Wen Cheng, Zhengyang Wu, and Luquan Ren

Cite This: ACS Omega 2024, 9, 43175−43183

Read Online

| ACCESS | | Metrics & More | | Article Recommendations |

ABSTRACT: The purpose of this paper is to develop a self-detecting diaphragm integrated with a flexible sensor, which is utilized in an underwater thruster. Resistive strain sensors are easy to manufacture and integrate due to their advantages in reliable stretchability and ductility. Inspired by the structure of neurons, we fabricated resistive flexible sensors using silica gel as the matrix with carbon black and carbon nanotubes as additives. All fabricated sensors demonstrated positive resistance characteristics under 60% strain conditions, with the sensor containing a mass ratio of 9 wt % carbon black and carbon nanotubes exhibiting the best resistance−strain linearity. To verify the anti-interference capability of sensors with silica gel substrates of varying hardness values under changing environmental pressure, we tested the pressure sensitivity of the sensors by altering the hardness of the silica gel. The results indicate that silica gel with the highest hardness value provides the best resistance to environmental pressure interference. To detect the motion and deformation of the internal functional components of the thruster, we combined strain detection with the movement operation function of a silica gel diaphragm, resulting in a new integrated diaphragm with sensor detection capabilities. The integrated diaphragm was evaluated by using a tensile testing machine and an LCR tester. The results demonstrate that the mechanical properties of the diaphragm are stable, exhibiting reliable resistance characteristics and a sensitive response during underwater operation. This research can also be applied to the detection of motion amplitudes of other types of soft robots.
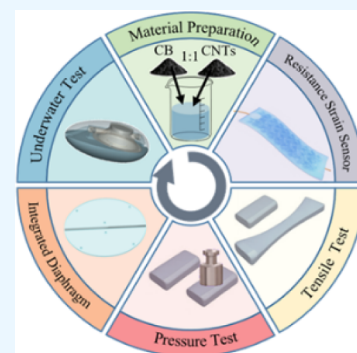
1. INTRODUCTION

With the increasing demand for an improved quality of life and advancements in sensing technology, various types of flexible sensors have been developed and utilized in fields, such as health monitoring[1,2] human−computer interaction,[3] artificial intelligence,[4] and intelligent manufacturing.[5] Compared with traditional rigid sensors, flexible sensors offer significant advantages, including versatile applications, scalability, and excellent biocompatibility. Strain sensors have emerged as one of the most widely used types of flexible sensors due to their simple structure and ability to convert physical deformation into resistance[6,7] and capacitance signals.[8,9] Based on different strain behaviors, strain sensors can be categorized into tensile strain sensors[10] and compressive strain sensors.[11] To fabricate these sensors, various materials have been explored, including metallic nanomaterials,[12,13] conductive polymers,[14] and carbon nanomaterials.[15] Flexible sensors made from metallic nanomaterials demonstrate high sensitivity;[16] however, their sensing range and tensile compression performance are limited. Conductive polymers exhibit poor stability and conductivity, which complicates the fabrication of high-performance sensors.[17] Carbon nanomaterials encompass carbon black,[18] carbon nanosheets,[19] nanotubes,[20] and graphene.[21] Among these, resistance strain sensors based on carbon black

elastomer nanomaterials have gained widespread use due to their ability to accommodate large deformations, high conductivity, and rapid resistance response. The resistance sensor reacts with tensile and compressive strains in six directions. The acquisition of the information to be detected is an urgent issue that needs to be addressed.[22,23]

In recent years, there has been increasing attention from experts and scholars to monitoring the working conditions of underwater thrusters, submersibles, and robots. The stretching, compression, bending, and other motion states of internal functional components, such as thrusters and submersibles, directly affect their propulsion and operational effectiveness.[24−26] Detecting the state of these key functional components is of great importance in the field of bionic propulsion. Traditional metal strain sensors are typically larger in size, and their installation process is time-consuming. As a result, they occupy a significant amount of internal space and

increase structural complexity, which introduces various inconveniences in the detection of flexible strain.[27,28] In contrast, flexible sensors can effectively identify and detect deformation or displacement states of different functional parts in a straightforward and efficient manner, which is crucial for promoting their practical application in monitoring the motion of underwater thrusters.[29] However, the working environment of underwater thrusters is very complex, characterized by high water pressure amplitudes with significant fluctuations,[30,31] necessitating enhanced anti-interference capabilities for flexible sensors. It is crucial to improve the strain detection sensitivity of these sensors for flexible functional components while simultaneously reducing their sensitivity to environmental water pressure.

In this article, we designed a propulsion device that mimics the squid, continuously drawing water from the front and expelling a jet of water from the back. The inner part of the device is divided into two chambers by a diaphragm. The up-and-down reciprocating motion of the diaphragm facilitates both the jetting and suction of the water flow. Additionally, the movement of the diaphragm directly influences the effectiveness of the propulsion system. To monitor the diaphragm's motion, we integrated flexible strain detection with the operational functionality of the silicone diaphragm, creating a diaphragm with sensor capabilities. We tested the mechanical properties and resistance characteristics of the diaphragm sensor by using a tensile testing machine and an LCR tester. The results indicate that the diaphragm's mechanical properties are stable, and the flexible sensor demonstrates reliable resistance characteristics under prolonged underwater working conditions, enabling effective detection of diaphragm motion.

2. EXPERIMENTAL SECTION

2.1. Material Preparation. Carbon black was sourced from Nanjing XFNANO Material Technology Co. Ltd., with a purity greater than 99.5% and particle size ranging from 27 to 40 nm. Carbon nanotubes were obtained from Hongdachang Evolution Technology Co. Ltd., featuring a diameter of 10 to 20 nm and a length of 5 to 15 μm. Considering the impact of silica gel hardness on the driving force of diaphragm motion in the double-chamber thruster function, and taking into account the maximum silicone hardness available on the market along with other factors, we selected silica gel with hardness ratings of 60, 40, and 20 A from Shenzhen Pusidun Silicone Material Co. Ltd. as the primary substrate for the sensor.

2.2. Production and Experimental Preparation of Strain Sensors. The resistance−strain sensor is composed of a carbon black carbon nanotube and a silica gel composite, which is prepared by means of a mechanical mixing method. The preparation steps for the strain sensor are illustrated in Figure 1. First, ensure that silica gel solvents A and B are added to the beaker in a 1:1 mass ratio through accurate weighing. Next, carbon nanotubes and carbon black powder, each with the same mass, are successively added to the mixed silica gel solution. Subsequently, the resulting mixture is then placed on an 85-2 magnetic agitator (produced by Changzhou Jintan Dadi Automation Instrument Factory) and initially homogenized at a speed of 1200 rad/min. Subsequently, the homogeneous solution is poured into a ball mill cup along with the added grinding balls. A KE-0.4 L ball mill (manufactured by Jiangsu Honghong Instrument and Equipment Co. Ltd.) is employed to mix the components for 20 min at a speed of 500 rad/min. This process yields a carbon black−

Figure 1. Resistance−strain sensor prepared by a mechanical mixing method.

carbon nanotube−silica gel nanocomposite solution, which is then degassed in air for 20 min before being poured into a mold. Finally, the mixture is cured at room temperature for 6 h, resulting in a silica-based strain sensor with dimensions of 70 mm × 20 mm × 2 mm.

To investigate the effect of the mass ratio of carbon black to carbon nanotubes on the mechanical properties and electrical conductivity of the sensor, a silica gel solution with a hardness of 60 A and a mass ratio of 1:1 for carbon black and carbon nanotubes was selected. Three resistance−strain sensors measuring $70 \times 20 \times 1 \ mm^3$ were then fabricated, and their tensile strength and resistance characteristics were tested. The DR-601A, produced by Dongri Instrument Company, was utilized for tensile testing of the resistance strain sensors. During the stretching process, the resistance of the sensor was recorded using a TH2830 LCR digital bridge tester manufactured by Changzhou Tonghui Electronics Co. Ltd. The 10 mm sections at both ends of the strain sensor were securely fixed to the upper and lower clips of the tensile testing machine. Wires were connected to both ends of the strain sensor to transmit resistance information to the LCR tester.

A strain sensor measuring 60 A and 9 wt % was fabricated by using the same process as described above. The sensor, with dimensions of $70 \times 20 \times 1 \ mms^3$, was attached to various parts of the body, including the shoulder, neck, fingers, knee, and foot, to detect human motion. Six experimental groups were designed and monitored to observe the corresponding changes in resistance associated with human joint movements.

2.3. Characterization and Tensile Performance Test of Strain Sensor. The maximum tensile displacement of the tensile testing machine is set to 30 mm, and the central 50 mm section of the strain sensor generated a tensile strain with a maximum strain rate of 60%. The upper chuck is extended at a speed of 20 mm/min. During the stretching process, the testing machine records the real-time relationship between the tension and tensile displacement. The stress−strain curve is illustrated in Figure 2a, while the resistance−strain curve is presented in Figure 2b. All three strain sensors exhibited excellent elastic deformation characteristics under the specified tensile conditions, which can be attributed to the inherent elasticity of the silica gel matrix. The tensile strength of the strain sensors increases with the concentration of carbon black and carbon nanotubes, indicating that the mechanical proper-
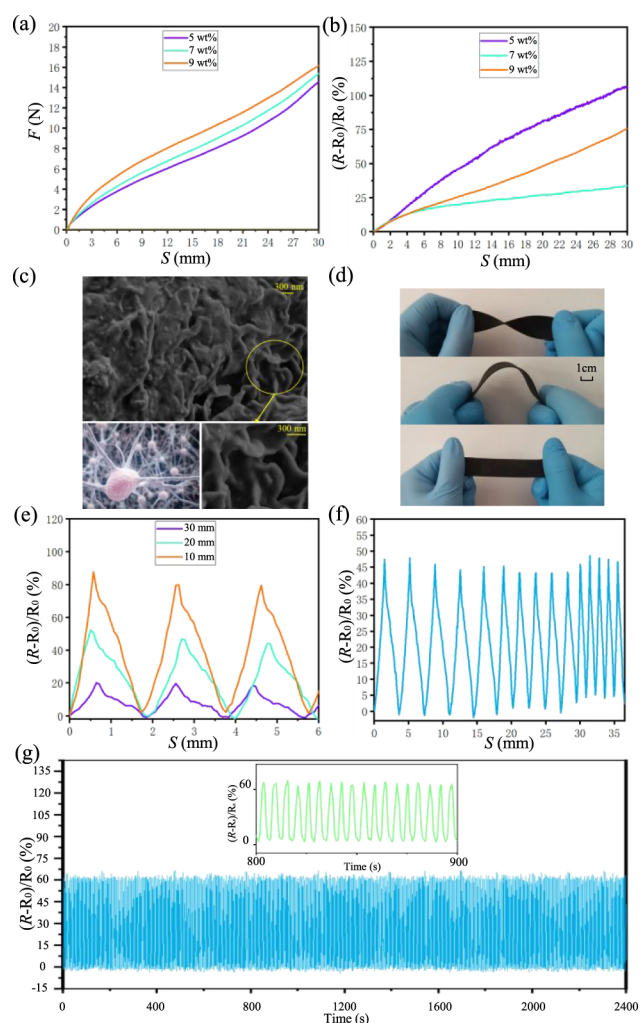
Figure 2. Strain sensor performance testing and characterization (a) Stress—displacement curves of three strain sensors. (b) Resistance—displacement curves of three strain sensors. (c) SEM images of cross sections of strain sensors with 9 wt % carbon black and carbon nanotubes content. (d) Tensile, bending, and torsion of resistance—strain sensors. (e) Tensile resistance—time curves of the same frequencies at different amplitudes. (f) Tensile resistance—time curves of different frequencies at the same amplitude. (g) Tensile resistance—time curve of the repeatability test at 50% tensile state.

ties of the strain sensors can be modulated by the mass percentage of the doped carbon black and carbon nanotubes. The initial resistance of strain sensors of the same size is 18.1 kΩ at a 5 wt % carbon black—carbon nanotube concentration, 6.8 kΩ at a 7 wt % concentration, and 450.0 Ω at a 9 wt % concentration. As the concentration of carbon black and carbon nanotubes increases, the conductivity of the carbon black carbon nanotube—silica gel sensor gradually improves. The resistance of each strain sensor increases almost linearly as the tensile displacement ranges from 0 mm to 30 mm, demonstrating stable performance over a wide testing range. When a sensor undergoes a deformation, such as tension or compression, the relative resistance $(R - R_0)/R_0$ (R and R_0 are the resistance magnitudes of the sensor in the deformed state and the initial state, respectively) will change accordingly.

The nervous system is the primary regulatory system in the human body, comprising numerous neurons. Neurons consist of somatic cells and neurites, with neurites further divided into dendrites and axons. Dendrites are one or more neurites that originate from somatic cells and have a radiating shape; their primary function is to receive stimuli and transmit impulses to somatic cells. Excitation is conveyed from one somatic cell to another neuron or tissue via an axon. To replicate the microstructure and versatility of neurons, carbon nanotubes and carbon black were selected as conductive materials. Carbon black simulates the structure of somatic cells, while carbon nanotubes mimic the structure of neurites. SEM images and neural structures depicted in Figure 2c demonstrate that the microstructure of the carbon nanotube and carbon black mixture closely resembles that of neurons. Carbon black, representing the cell body of a neuron, connects to multiple carbon nanotubes that serve as protrusions. This configuration creates additional conductive pathways within the sensor, facilitating changes in the internal conductor's state when strain is applied due to external forces, thereby enhancing its sensitivity. Figure 2d illustrates the actual appearance of the strain sensor and its ability to be stretched, bent, and twisted, showcasing the excellent deformation properties of the sensor. To assess the stability of the strain sensor, we stretched it from 0 to 10 mm (and subsequently to 20 and 30 mm) along its length within one second. After stretching, the sensor was allowed for 1 s to return to its initial length, and this cycle was repeated, with three cycles being recorded. The resistance curve plotted over time is presented in Figure 2e. In the three different tensile states, the resistance values exhibited significant variation, indicating that the tensile strain variable of the sensor can be characterized by changes in the resistance. Under the same tensile amplitude, the resistance values of the sensor followed a consistent trend, reflecting the sensor's stability. During the process of applying tensile strain at three different speeds to achieve the same tensile strain (0 to 20 mm) over a total of 15 cycles, the trend of resistance change over time is illustrated in Figure 2f. In the process of stretching the strain sensor at a constant speed to achieve a consistent tensile strain of 0 to 25 mm over a total of 450 cycles, the trend of resistance change over time is illustrated in Figure 2g. The periodicity of the resistance change remained stable throughout the testing process, demonstrating the sensor's reliability and stability.

The experimental results indicate that the sensor containing 9 wt % carbon black and carbon nanotubes exhibits the best linear characteristics. Consequently, three strain sensors were fabricated using a silica gel substrate with hardness values of 20, 40, and 60 A, combined with carbon black and carbon nanotubes at a mass ratio of 9 wt %. Each sensor measured 70 mm × 20 mm × 2 mm, and their stress—strain curves are presented in Figure 3a. During the stretching process, the stress in all three sensors increases as the stretching distance increases. Under identical strain conditions, the tensile strength of the sensors increases with the hardness of the silica gel substrate. The resistance—strain curves for each strain sensor display a similar trend, as illustrated in Figure 3b. The sensitivity of the strain sensor with a 60 A hardness is approximately 13.83 Ω/mm. These results suggest that variations in the hardness of the silica gel substrate have a minimal impact on the resistance values of the strain sensors.

The sensor designed in this paper is intended for use in environments with complex variations in ambient pressure. Changes in ambient pressure on the sensor's surface induce compressive deformation in the strain sensor.[32] This compressive deformation alters the sensor's resistance, which
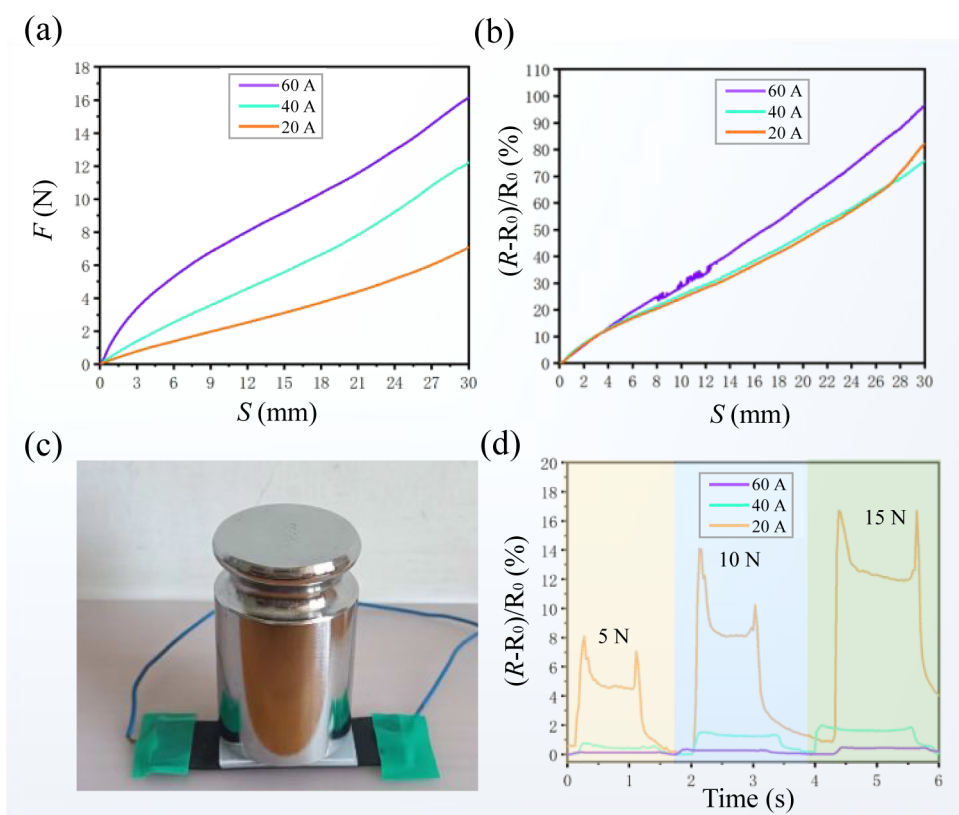
Figure 3. Piezo-resistive characteristic test of resistive sensor.(a) Stress−displacement characteristic curves of silicone resistance sensors with different hardness. (b) Resistance−displacement characteristic curves of silicone resistance sensors with different hardness. (c) Weight test piezo-resistive characteristic test of sensor. (d) Piezo-resistive characteristic curves of three sensors under different hardness of silica gel.

can interfere with the measurement of tensile strain along the sensor's length. It is essential to ensure the tensile strain performance of the sensor, while minimizing its sensitivity to environmental pressure. To address this, we tested the piezoresistive characteristics of three strain sensors constructed from silica gel substrates with Shore A hardness ratings of 20, 40, and 60 A. As illustrated in Figure 3c, weights of varying magnitudes 5, 10, and 15 N were successively applied in the thickness direction of a 40×20 mm^2 square area located at the center of the three strain sensors. The pressure−resistance characteristic curves for these sensors are presented in Figure 3d. Among the three strain sensors, the one made from 60 A silica gel exhibited the greatest resistance to pressure interference. Consequently, the 60 A (9 wt %) strain sensor demonstrated linear strain−resistance characteristics and superior pressure resistance, making it well-suited for strain detection applications in high-pressure environments and offering promising prospects for widespread use.

2.4. Human Motion Detection of Strain Sensor. Based on the above-mentioned advantages of the product, including rapid response capability, wide and stable detection range, and excellent durability, it is applied to the sensor for human movement monitoring. The shoulder joint serves as the connection between the upper limb and the trunk, providing support and stability to the upper limb. Additionally, it is one of the joints frequently utilized during exercise in our daily lives, making it a crucial component of human motion. We affixed a prepared sensor to the shoulder joint and connected both ends of the sensor to an LCR to assess the arm's motion from a horizontal position to a vertical orientation, and then back to the original level. The maximum range of motion for

the shoulder joint is approximately 90°, while the maximum strain variable of the sensor is about 15 mm. The resistance−time characteristic curve is illustrated in Figure 4a. As a vital structure that supports the head, the cervical spine possesses a certain degree of flexibility. The cervical vertebrae are essential for various daily activities, such as nodding, lifting the head, and rotating the left and right. To detect the motion characteristics of the cervical spine, a strain sensor was attached to the back of the neck for testing. Throughout the entire movement process, the individual first maintains an upright neck position while looking ahead, then bends the neck down to gaze directly at the feet, and subsequently lifts the head and neck back to an upright position. During this cycle, the resistance−time curve for five cycles was recorded, as shown in Figure 4b. Fingers, which are the distal parts of the human body, consist of bone, muscle, nerves, and other tissues and exhibit a high degree of flexibility. The finger joints comprise the proximal phalanx, middle phalanx, and distal phalanx, allowing for flexion, extension, and gripping. A strain sensor was attached to the exterior of a human index finger, encompassing the middle phalanx and the two adjacent joints. The trend in resistance change of the sensor was monitored as the finger bent. Initially, the bent finger transitioned from a completely straight position to a slightly bent position, holding for 2 s. Next, the finger moved from a slightly bent position to a state of less than "90°" and held for 3 s before continuing to bend into a clenched fist position and holding for another 2 s. The resistance−time characteristic curve of the sensor throughout this process is depicted in Figure 4c. The resistance change trend of the sensor clearly indicates the degree of finger curvature. The elbow joint plays a crucial role in transferring
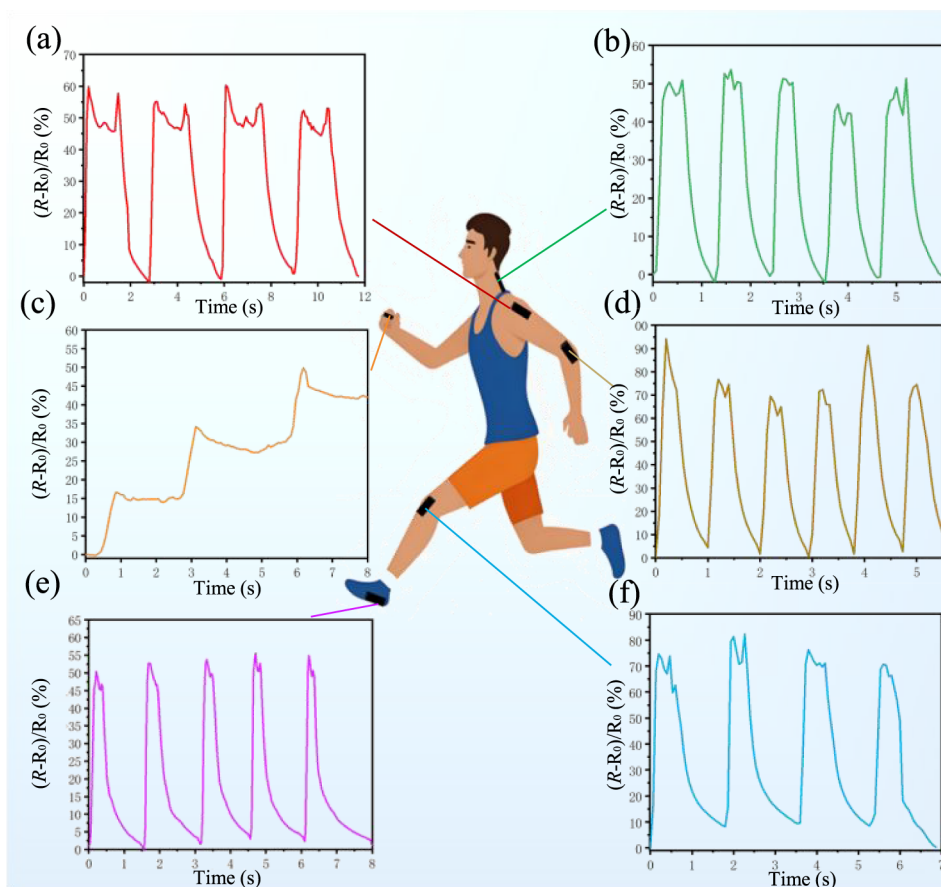
Figure 4. Human movement signal detection: (a) shoulder bend test, (b) neck bend test, (c) finger bend test, (d) elbow bend test, (e) walking pressure test, and (f) knee bend test.

force, assisting movement, supporting weight, protecting soft tissue, and enhancing stability. The primary movements of the elbow joint include flexion and extension. Flexion refers to the bending and contraction of the forearm, which corresponds to the action of lifting objects in daily life. Extension, on the other hand, involves straightening the forearm, corresponding to the action of pushing and extending objects commonly encountered in daily activities. To detect elbow movement, we attach a strain sensor to the outer side of the elbow joint. The elbow is initially positioned in a straight line, then bent to approximately 150°, and subsequently straightened again. The maximum motion observed is about 30 mm, and this process is repeated for six cycles. The resistance−time change curve of the strain sensor is illustrated in Figure 4d. Walking is one of the fundamental forms of human activity and is widely regarded as the most beneficial movement for overall health; it appears that the entire human body structure is optimized for walking. A subject weighing 85 kg was selected for measurement with the strain sensor fixed under the left foot. The sensor recorded signals over five cycles while the subject walked a distance of 10 m at a normal pace, as shown in Figure 4e. The resistance values exhibited periodic changes, confirming the stability of the strain sensor's pressure detection performance. Squatting is a form of leg muscle exercise that serves as an effective aerobic workout. It can enhance cardiopulmonary function, reduce body fat, prevent osteoporosis, and improve mental well-being, making it a primary mode of fitness training. Figure 4f presents the resistance−time characteristic curve recorded during the squatting motion.

Throughout the exercise, individuals transition from a standing position to a complete squat and then rise again, repeating this cycle, while intercepting signals over four squatting cycles. The resistance−time curve of the strain sensor effectively reflects the entire process of the squatting motion.

The six groups of tests demonstrate that the strain sensor is effective for detecting a wide range of human motions. It is characterized by its ease of use, flexibility, and straightforward preparation process.

3. MANUFACTURING AND TESTING OF UNDERWATER THRUSTER FUNCTION DIAPHRAGM

A chamber in the cuttlefish known as the mantle chamber functions as a pressure chamber. This chamber features two openings: a larger one, referred to as the mantle aperture, and a smaller one, called the funnel tube, both oriented in the same direction. During the process of water jet propulsion, the mantle aperture closes, while the funnel tube opens, creating a jet. In the water absorption phase, the mantle chamber expands, allowing water to be drawn into the mantle chamber through the mantle aperture.[33]

Combined with the biological functions and deformation modes of the cuttlefish, the analysis revealed that the water absorption process of the cuttlefish generates additional resistance and energy consumption. We propose that if we can achieve unidirectional water flow during the suction and drainage cycles, the propulsion efficiency can be enhanced. A novel suction and drainage propulsion system is proposed in
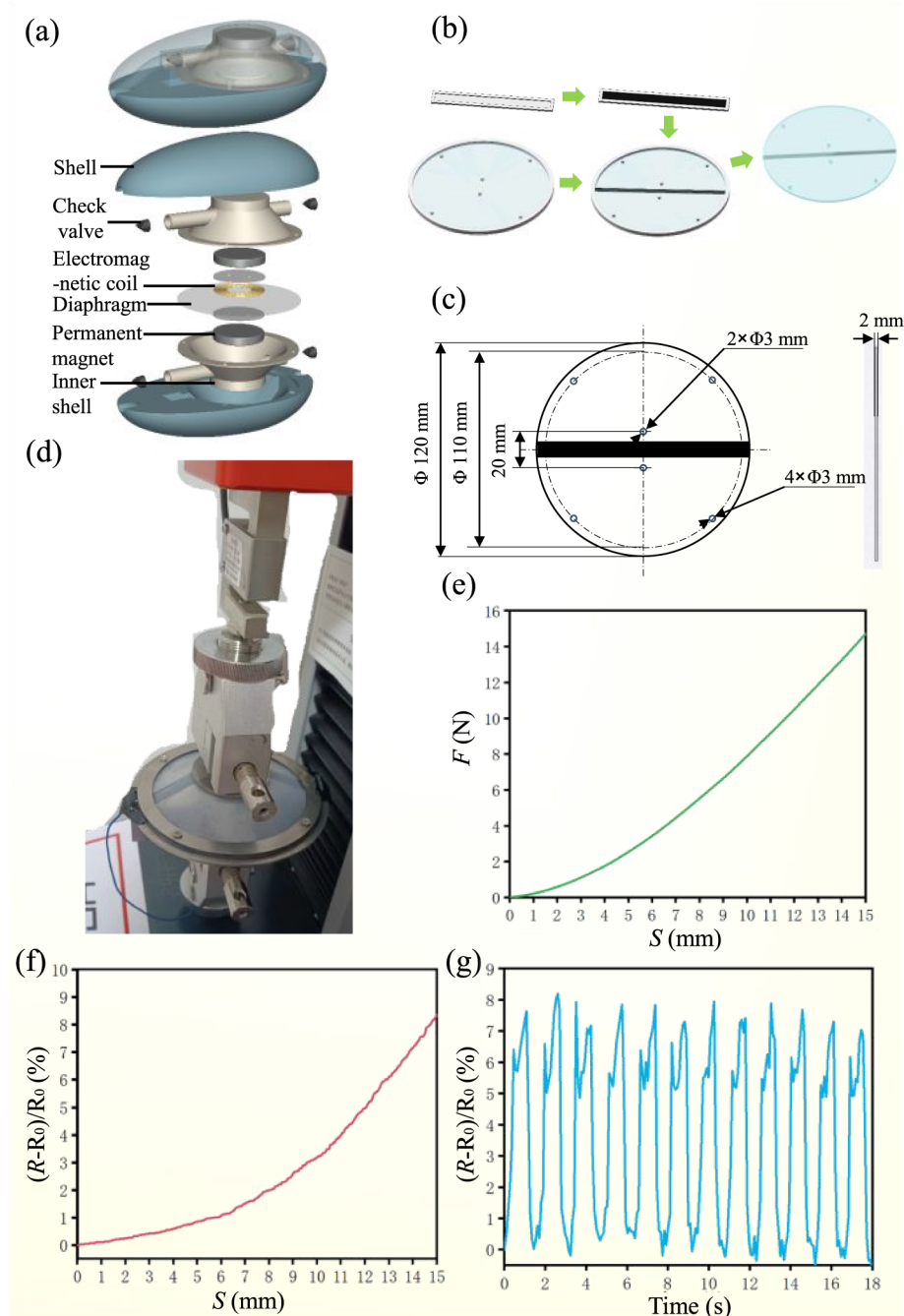
Figure 5. Manufacturing and performance testing of functional integrated diaphragm. (a) Schematic diagram of the thruster structure. (b) Fabrication process of the integrated diaphragm. (c) Detailed dimensions of the integrated diaphragm. (d) Tensile test of the integrated diaphragm. (e) Stress−strain curve of the integrated diaphragm. (f) Resistance−displacement curve during the diaphragm stretching process. (g) Resistance−time curve of the diaphragm during the operation of the thruster.

which the water inlet is positioned at the front end of the thruster, while the water outlet is located at the back end. The outer shell of the thruster is ellipsoidal, and the inner chamber consists of two circular hollow inner shells. A diaphragm separates the inner chamber, forming a double chamber. An electromagnetic coil is mounted in the center of the diaphragm. Two cylindrical permanent magnets are fixed between the outer shells and the inner shells. The electro-magnetic force drives the diaphragm to move up and down, altering the volume of the double chamber, allowing the thruster to alternately expel water.[34] As illustrated in Figure 5a, the upper image is a schematic diagram of the double chamber

thruster, while the lower image is an exploded view of the main functional components of the thruster. The thruster comprises two outer shells, two inner shells, two permanent magnets, one diaphragm, one electromagnetic coil, two baffles, and two bolts to ensure that the electromagnetic coil and diaphragm are securely fixed together. One end of the inner shell serves as an outlet pipe, while the other end functions as an inlet pipe, with a check valve installed at the pipe's port. The electromagnetic coil and silicone diaphragm form a moving component, with the electromagnetic coil driving the silicone diaphragm to move up and down under the influence of an electromagnetic force. By controlling the direction of the current, the magnetic

field exerts an upward force on the electromagnetic coil. This action causes the silicone diaphragm to move upward, reducing the internal volume of the upper chamber, which allows water in the upper chamber to flow to the left and be discharged outside the chamber. The inner volume of the lower chamber increases, causing water from outside the chamber to flow in through the right check valve. When the direction of the current is reversed, the magnetic field generates a downward force on the electromagnetic coil. This coil then drives the silicone diaphragm downward, which increases the internal volume of the upper chamber, allowing water from the outside to flow into it from the right. As the internal volume of the lower chamber decreases, the water within it flows to the left and drains outside. By periodically reversing the direction of the current, the process of alternating water injection in the doublechamber is achieved, resulting in continuous forward propulsion of the double-chamber thruster.

The target application for this thruster is an underwater environment. However, the reliability of conventional contact sensors cannot be guaranteed when used underwater. Therefore, our designed flexible sensor will be utilized to monitor the operating conditions of the underwater thruster.

According to the requirements for motion state detection in a double-chamber thruster diaphragm, an integrated strain detection diaphragm was designed and fabricated. The specific manufacturing steps for the integrated diaphragm are illustrated in Figure 5b. First, a resistance strain sensor measuring 120 mm in length, 10 mm in width, and 1 mm in thickness was created using 60 A silica gel as the base, combined with a mass ratio of 9 wt % carbon black and carbon nanotubes. Next, 5.6 mL of 20 A silica gel solution was poured into the inner chamber of a mold with a diameter of 120 mm and a depth of 2 mm and allowed to solidify for 5 h at room temperature. Subsequently, the flexible sensor was positioned in the flat, symmetrical center of the mold, and 16.4 mL of 20 A silicone solution was poured into the mold chamber, which also underwent a solidification process lasting 5 h at room temperature. The resulting integrated functional diaphragm, with a thickness of 2 mm, features an internal strain sensor insulated with 20 A of silicone. The specific dimensions of the integrated diaphragm are depicted in Figure 5c.

The exterior of the integrated diaphragm is secured by two circular ring clips, which have an external diameter of 120 mm and an internal diameter of 100 mm. Additionally, two circular clips with diameters of 50 mm are affixed to the central region of the integrated diaphragm. The ring clips and the circular clips are attached to the upper and lower clamps of the tensile testing machine, as illustrated in Figure 5d. The tensile testing machine was employed to evaluate the stress−strain characteristics of the diaphragm, while an LCR meter was utilized to assess the resistance−strain characteristics. The results of the tension−displacement tests are presented in Figure 5e. As the tensile strain increases, the tensile stress of the diaphragm also rises. The resistance−strain curve is depicted in Figure 5f, showing that the resistance value increases with the elongation of the diaphragm due to the tensile strain.

To investigate the motion and detection capabilities of the integrated functional diaphragm, we set the driving current of the electromagnetic coil at 10 A. A 2 min underwater propulsion test was conducted, during which signals corresponding to 18 s and 6 motion cycles were recorded. The resistance−time characteristic curve of the diaphragm sensor was plotted, as illustrated in Figure 5g. The motion

range of the diaphragm in the double-chamber propeller was observed to be 15 mm in both upward and downward directions. The resistance measurements indicated that the diaphragm moved upward 6 times and downward 6 times within the 18 s interval, each time reaching a position close to 15 mm. This data reveals a periodic variation in resistance, which aligns with the resistance characteristic curve shown in Figure 5f, thereby confirming the durability and stability of the functional diaphragm, as well as its strain detection performance. As illustrated in Figure 5g, a single movement period reveals that the diaphragm undergoes three distinct stages during deformation. The first stage involves rapid deformation from the planar state, primarily because the electromagnetic force significantly exceeds both the elastic force of the diaphragm and the reaction force of the water. The diaphragm then deforms to its maximum strain state at a slower rate, as the growth rate of the diaphragm's elastic force surpasses that of the electromagnetic force, leading to a reduction in the diaphragm's motion speed. Finally, the diaphragm swiftly recovers from the maximum deformation state back to the planar state, with the deformation speed being the highest when both the electromagnetic force and the diaphragm's elastic force perform positive work simultaneously.

Consequently, we conclude that the integrated diaphragm that we designed can move stably underwater. The strain detection capability of the integrated diaphragm effectively characterizes the deformation process and motion state of the diaphragm in aquatic environments. Our strain sensors can be integrated into functional components and are suitable for strain detection in scenarios involving significant pressure changes. For instance, they can be utilized in underwater thrusters, bionic fish, and equipment for deep sea research, marine environment monitoring, and marine resource development, among other applications.[35]

4. RESULTS AND DISCUSSION

This article develops a diaphragm for the self-detection of strain in underwater thrusters. In this study, a flexible strain diaphragm composed of elastomer composites containing carbon black and carbon nanotubes is proposed. This diaphragm is designed for use in underwater environments, where pressure fluctuations are complex, and significant strains can occur. The resistance of the strain sensors decreases as the concentration of carbon black and carbon nanotubes increases. The strain sensor with a 9 wt % concentration of carbon black and carbon nanotubes exhibits the best resistance−strain linearity. To evaluate the sensors' resistance to pressure interference, we prepared three strain sensors using silica gel substrates of varying hardness. As the hardness of the silica gel decreases, the sensor's sensitivity to pressure increases. Piezoresistive testing demonstrates that the strain sensor made from 60 A silica gel possesses a high capacity to resist pressure interference. The practicality and reliability of the sensor were verified by monitoring six different human motion behaviors. We fabricated a strain sensor with a 9 wt % concentration of carbon black and carbon nanotubes on a 60 A silica gel substrate, integrating the sensor within a 20 A silica gel diaphragm. This integrated diaphragm, which features strain detection capabilities and strong resistance to environmental pressure interference, was installed in a double-chamber water jet propulsion device. The motion state of the integrated diaphragm can be monitored, while the thruster operates via water jet propulsion. In conclusion, we have developed a

flexible strain sensor that demonstrates significant strain capacity and resistance to pressure interference, making it suitable for detecting strain in subsea propulsion structures.

■ AUTHOR INFORMATION

Corresponding Author

Chengchun Zhang − *Key Laboratory of Bionic Engineering (Ministry of Education), Jilin University, Changchun 130022, China; Weihai Junming Power Technology Co., Ltd., Weihai 264200, China;* ⓞ orcid.org/0000-0002-0930-1139; Email: jluzcc@jlu.edu.cn

Authors

Chong Cao − *Key Laboratory of Bionic Engineering (Ministry of Education), Jilin University, Changchun 130022, China;* ⓞ orcid.org/0009-0009-4012-3332

Chun Shen − *Weihai Junming Power Technology Co., Ltd., Weihai 264200, China; College of Automotive Engineering, Jilin University, Changchun 130022, China*

Yasong Zhang − *Key Laboratory of Bionic Engineering (Ministry of Education), Jilin University, Changchun 130022, China*

Wen Cheng − *Key Laboratory of Bionic Engineering (Ministry of Education), Jilin University, Changchun 130022, China*

Zhengyang Wu − *Key Laboratory of Bionic Engineering (Ministry of Education), Jilin University, Changchun 130022, China*

Luquan Ren − *Key Laboratory of Bionic Engineering (Ministry of Education), Jilin University, Changchun 130022, China*

Complete contact information is available at:
https://pubs.acs.org/10.1021/acsomega.4c07358

Notes

The authors declare no competing financial interest.

■ REFERENCES

(1) Hu, J.; Dun, G.; Geng, X.; Chen, J.; Wu, X.; Ren, T.-L. Recent progress in flexible micro-pressure sensors for wearable health monitoring. *Nanoscale Adv.* **2023**, *5* (12), 3131−3145.

(2) Sonil, N. I.; Ullah, Z.; Chen, J.; Wang, G. P. Wearable strain sensors for human motion detection and health monitoring based on hybrid graphite-textile flexible electrodes. *J. Mater. Res. Technol.* **2023**, *26*, 764−774.

(3) Gajula, P.; Yoon, J. U.; Woo, I.; Oh, S.-J.; Bae, J. W. Triboelectric touch sensor array system for energy generation and self-powered human-machine interfaces based on chemically functionalized, electrospun rGO/Nylon-12 and micro-patterned Ecoflex/MoS2 films. *Nano Energy* **2024**, *121*, 109278.

(4) Prabhu, M. R.; Sivaraman, R.; Nagabhooshanam, N.; Kumar, R. S.; Salunkhe, S. S. Empowering artificial intelligence-based multi-biometric image sensor for human identification. *Meas.: Sens.* **2024**, *33*, 101082.

(5) Won, S.; Won, K. Self-powered flexible oxygen sensors for intelligent food packaging. *Food Packag. Shelf Life* **2021**, *29*, 100713.

(6) Yu, Z.; Xu, J.; Gong, H.; Li, Y.; Li, L.; Wei, Q.; Tang, D. Bioinspired self-powered piezoresistive sensors for simultaneous monitoring of human health and outdoor UV light intensity. *ACS Appl. Mater. Interfaces* **2022**, *14* (4), 5101−5111.

(7) Zazoum, B.; Batoo, K. M.; Khan, M. A. A. Recent advances in flexible sensors and their applications. *Sensors* **2022**, *22* (12), 4653.

(8) Ha, K.-H.; Zhang, W.; Jang, H.; Kang, S.; Wang, L.; Tan, P.; Hwang, H.; Lu, N. Highly sensitive capacitive pressure sensors over a wide pressure range enabled by the hybrid responses of a highly porous nanocomposite. *Adv. Mater.* **2021**, *33* (48), 2103320.

(9) Kurnaz, S.; Ozturk, O.; Mehmet, A. H.; Guduloglu, U.; Yilmaz, N.; Cicek, O. Flexible capacitive and piezoresistive pressure sensors based on screen-printed parylene C/polyurethane composites in low-pressure range. *Flexible Printed Electron.* **2023**, *8* (3), 035015.

(10) Zhu, X.; Wan, T.; Chen, M.; Wang, S.; Zhang, Y.; Yuan, G.; Liu, X.; Cheng, B. Micro-wrinkled rGO/PU aerogel as flexible strain sensor preparing for motion detection and voice recognition. *J. Alloys Compd.* **2023**, *954*, 170185.

(11) Yang, Y.; Song, W.; Murugesan, B.; Cheng, X.; Jiang, M.; Chen, Z.; Yan, B.; Cai, Y. Oriented Ti3C2Tx MXene-doped silk fibroin/hyaluronic acid hydrogels for sensitive compression strain monitoring with a wide resilience range and high cycling stability. *Colloids Surf., A* **2023**, *665*, 131221.

(12) Raman, S.; Arunagirinathan, R. S. Silver nanowires in stretchable resistive strain sensors. *Nanomaterials* **2022**, *12* (11), 1932.

(13) Xing, L.; Wang, X.; Li, M.; Jia, Y.; Yang, G.; Liu, C.; Shen, C.; Liu, X. Self-adhesive, stretchable waterborne polyurethane-based flexible film as wearable conformal strain sensor for motion and health monitoring. *Adv. Nanocompos.* **2024**, *1* (1), 171−179.

(14) Tran, V. V.; Lee, S.; Lee, D.; Le, T.-H. Recent developments and implementations of conductive polymer-based flexible devices in sensing applications. *Polymers* **2022**, *14* (18), 3730.

(15) Yoo, J.; Kim, D.-Y.; Kim, H.; Hur, O.-N.; Park, S.-H. Comparison of pressure sensing properties of carbon nanotubes and carbon black polymer composites. *Materials* **2022**, *15* (3), 1213.

(16) Huang, Z.; Yu, S.; Xu, Y.; Cao, Z.; Zhang, J.; Guo, Z.; Wu, T.; Liao, Q.; Zheng, Y.; Chen, Z.; et al. In-Sensor Tactile Fusion and Logic for Accurate Intention Recognition. *Adv. Mater.* **2024**, *36* (35), 2407329.

(17) Liu, G.; Zhang, Z.; Li, Z.; Guo, L.; Ning, L. 0D to 2D carbon-based materials in flexible strain sensors: Recent advances and perspectives. *2D Mater.* **2023**, *10* (2), 022002.

(18) Zhu, Y.; Chen, X.; Chu, K.; Wang, X.; Hu, Z.; Su, H. Carbon black/PDMS based flexible capacitive tactile sensor for multi-directional force sensing. *Sensors* **2022**, *22* (2), 628.

(19) Bao, S.; Gao, J.; Xu, T.; Li, N.; Chen, W.; Lu, W. Anti-freezing and antibacterial conductive organohydrogel co-reinforced by 1D silk nanofibers and 2D graphitic carbon nitride nanosheets as flexible sensor. *Chem. Eng. J.* **2021**, *411*, 128470.

(20) Cao, X.; He, T.; Sui, J.; Yan, Y.; Liu, X.; Liu, L.; Lv, S. PVA/KGM dual network hydrogels doped with carbon nanotube-collagen corona as flexible sensors for human motion monitoring. *J. Mater. Chem. C* **2024**, *12* (9), 3333−3344.

(21) Hairi, N. I. I. M.; Ralib, A. A. M.; Ahmad, F. B.; Hattar, M. A. B. M. Synthesis and characterization of different graphite/chitosan ink ratio composition towards flexible strain sensor performance. *J. Mater. Sci.: mater. Electron.* **2022**, *33*, 15574−15585.

(22) Chen, Z.; Lin, W.; Zhang, C.; Xu, Y.; Wei, C.; Hu, H.; Liao, X.; Chen, Z. Multifunctional and reconfigurable electronic fabrics assisted by artificial intelligence for human augmentation. *Adv. Fiber Mater.* **2024**, *6* (1), 229−242.

(23) Wei, C.; Lin, W.; Wang, L.; Cao, Z.; Huang, Z.; Liao, Q.; Guo, Z.; Su, Y.; Zheng, Y.; Liao, X.; et al. Conformal Human−Machine Integration Using Highly Bending-Insensitive, Unpixelated, and Waterproof Epidermal Electronics Toward Metaverse. *Nano-Micro Lett.* **2023**, *15* (1), 199.

(24) Chowdhury, S. A.; Saha, M. C.; Patterson, S.; Robison, T.; Liu, Y. Highly conductive polydimethylsiloxane/carbon nanofiber compo-

sites for flexible sensor applications. *Adv. Mater. Technol.* **2019**, *4* (1), 1800398.

(25) Jeong, C.-S.; Kim, G.; Lee, I.; Jin, S. Empirical modeling of 2-degree-of-freedom azimuth underwater thruster using a signal compression method. *Appl. Sci.* **2021**, *11* (8), 3517.

(26) Zhang, R.; Shen, Z.; Zhong, H.; Tan, J.; Hu, Y.; Wang, Z. A cephalopod-inspired soft-robotic siphon for thrust vectoring and flow rate regulation. *Soft Rob.* **2021**, *8* (4), 416−431.

(27) Gai, N.; Zhang, M.; Liu, X. Fault feature extraction method for AUV thruster based on two-stage fusion from multi-source information. *Ocean Eng.* **2024**, *294*, 116738.

(28) Xu, G.; Guo, W.; Zhao, Y.; Zhou, Y.; Zhang, Y.; Liu, X.; Xu, G.; Li, G. Online learning based underwater robotic thruster fault detection. *Appl. Sci.* **2021**, *11* (8), 3586.

(29) Gong, T.; Shao, H.-Q.; Sun, X.-R.; Guo, J.-X.; Hou, J.-R.; Ke, K.; Gong, L.; Cao, Y.; Cao, Y.-H.; Bao, R.-Y.; Yang, W. Spatial hetero-structured composites with ultrawide linear range for positive-negative pressure sensing and e-skin of bionic fish. *Nano Energy* **2024**, *120*, 109173.

(30) Zhou, X.; Chen, W.; Zheng, H.; Liu, B.; Liu, J.; Li, K. A novel anti-hydropressure piezoelectric jetting micro thruster for steering AUV. *Int. J. Mech. Sci.* **2024**, *262*, 108737.

(31) Li, J.; Wang, Y.; Li, H.; Liu, X.; Chen, Z. Sliding Mode Control with Adaptive-Reaching-Law-Based Fault-Tolerant Control for AUV Sensors and Thrusters. *J. Mar. Sci. Eng.* **2023**, *11* (11), 2170.

(32) Chen, Q.; Gao, Q.; Wang, X.; Schubert, D. W.; Liu, X. Flexible, conductive, and anisotropic thermoplastic polyurethane/polydopamine/MXene foam for piezoresistive sensors and motion monitoring. *Compos., Part A* **2022**, *155*, 106838.

(33) Zhu, Q.; Xiao, Q. Physics and applications of squid-inspired jetting. *Bioinspiration Biomimetics* **2022**, *17* (4), 041001.

(34) Cao, C.; Zhang, Y.; Zhang, C.; Shen, C.; Cheng, W.; Wei, Z.; Wu, Z.; Ren, L. Design of bionic water jet thruster with double-chamber driven by electromagnetic force. *Int. J. Mech. Syst. Dyn.* **2024**, *4*, 292−302.

(35) Sun, G.; Wang, P.; Jiang, Y.; Sun, H.; Liu, T.; Li, G.; Yu, W.; Meng, C.; Guo, S. Bioinspired flexible, breathable, waterproof and self-cleaning iontronic tactile sensors for special underwater sensing applications. *Nano Energy* **2023**, *110*, 108367.